ADVANCED FUNCTIONAL MATERIALS
www.afm-journal.de

Quasi-Three-Dimensional Angle-Tolerant Electromagnetic Illusion Using Ultrathin Metasurface Coatings

*Zhi Hao Jiang and Douglas H. Werner**

Low-profile and light-weight coatings that offer comprehensive manipulation of the electromagnetic scattering for finite-length objects are highly desirable, but not yet achieved, for applications including camouflaging, deceptive sensing, radar cognition control, and defense security. Here, for the first time, the theory, practical design, and experimental demonstration of quasi-three-dimensional and angle-tolerant electromagnetic illusion coatings are presented which have been enabled by ultrathin single-layer functional metasurfaces. By controlling the multiple Mie scattering coefficients using the tangential and non-vanishing radial electromagnetic responses of the metasurface, the quasi-two-dimensional coating transforms the electromagnetic perception of one object to mimic that of another which has been pre-selected by the designer. The illusion coating, which is homogeneous but anisotropic, is realized using hundreds of composite electric and magnetic sub-wavelength unit cells operating at frequencies away from their resonance. Two different prototypes of the metasurface illusion coatings were fabricated and characterized, demonstrating very good camouflaging performance for finite-length dielectric as well as conducting objects within a field-of-view up to ±10° off normal. This work paves the way for practical artificially engineered material coatings with exotic and versatile scattering control capabilities that would enable a wide range of applications throughout the entire electromagnetic spectrum.

1. Introduction

The unusual electromagnetic properties of functional metamaterials,[1–3] which arise from their engineered electric and/or magnetic building blocks on a subwavelength scale, have revolutionized the way scientists and engineers can manipulate the electromagnetic perception of objects, resulting in a variety of devices with unconventional scattering control functionalities, including invisibility cloaking,[4–21] optical illusion,[22–27] and so on. Among these, cloaking can be considered as a special case of illusion optics where the scattering signature of an object is suppressed to mimic that of free space. In general, two routes have been investigated for developing artificially engineered material coatings to achieve exotic scattering manipulation – the transformation optics (TO) approach[3] and the scattering cancellation method.[28] The TO-enabled coatings rely on the form invariant property of Maxwell's equations such that the waves can be bent almost arbitrarily according to specially designed coordinate mappings, resulting in transformed media that often require inhomogeneous and/or anisotropic material properties.[29,30] It has been demonstrated that invisibility cloaking and the more general illusion optics phenomena can be accomplished using multilayer metamaterial coatings or two dimensional transmission line networks.[5,6,23–27] However, these cloaking and illusion coatings usually have form factors comparable to or even much larger than the size of the coated objects, leading to a bulky volume along with a noticeable amount of absorption loss. In addition, due to the singularity associated with most coordinate transformations employed for cloaking and illusion, the region inside the coatings is isolated from the outside, which excludes the possibility for communication between the two regions. This makes such coatings unfavorable for applications where the coated object is a sensor or an antenna.[11,12] Moreover, in addition to the performance degradation when these multilayer TO-enabled metamaterial cloaking and illusion coatings are truncated to have a practical finite length, their electromagnetic properties are also sensitive to a variation in the angle of incidence.[31,32]

The scattering cancellation method provides an alternative pathway towards electromagnetic invisibility and transparency by suppressing the magnitude of the Mie scattering coefficients of the coated objects.[33] In early work, homogenous and inhomogeneous coatings containing negative or low permittivity materials have been proposed theoretically and verified experimentally to achieve near-zero radar cross section (RCS).[12–16] It has been shown that the transparency is made possible when the induced dipole moments of the coated-object and the coating are out of phase and equal in magnitude, thereby cancelling their contributions in both the near- and far-field regions. Importantly, such scattering cancellation based cloaking coatings allow for non-vanishing fields and/or currents to be induced on the coated object, which makes them more amenable than TO-enabled cloaks for applications such as scattering reduction of sensors and noninvasive probing. More recently, ultrathin cloaking coatings have been proposed

Z. H. Jiang, D. H. Werner
Department of Electrical Engineering
The Pennsylvania State University
University Park, PA 16802, USA
E-mail: dhw@psu.edu

DOI: 10.1002/adfm.201401561

and demonstrated using quasi-two-dimensional metamaterials comprised by only a monolayer of patterned sub-wavelength metallic resonators,[19–21] which are also referred to as metasurfaces.[34,35] These metasurface-based cloaks have significant practical advantages over bulk material coatings due to their low profile and conformal properties. More recently it has also been shown that when the non-vanishing radial component of the anisotropic metasurface is properly exploited, a near-perfect cloaking effect can be achieved for objects beyond the quasi-static limit with only a single-layer metasurface coating.[36] However, a systematic methodology for achieving more advanced scattering manipulation, which goes further than simply suppressing the scattered fields, has not yet been theoretically proposed or experimentally validated using low-profile metasurface coating technology.

In this paper, we theoretically predict and experimentally demonstrate, for the first time, quasi-three-dimensional angle-tolerant electromagnetic illusion effects for objects with finite-length using ultrathin single-layer anisotropic metasurface coatings. It is shown that by properly tailoring the superficial electromagnetic properties of a metasurface, the scattering response of a coated dielectric cylinder can be transformed into mimicking that of an uncoated conducting cylinder, and vice versa. Importantly, the metasurface coating is optimized to control both the zeroth- and first-order complex Mie scattering coefficients, thereby generating illusion within a certain angular range for finite-length cylinders with practical diameters as large as $0.3\lambda_0$, which is beyond the quasi-static limit. Two proof-of-concept metasurface illusion coating prototypes are fabricated and characterized, experimentally achieving RCS patterns of the metasurface coated objects resembling those of the targeted ones within a field-of-view up to ±10° off normal.

2. Scattering Manipulation Using Anisotropic Metasurface Coatings

The functionality of the ultrathin metasurface illusion coating is illustrated in **Figure 1**, which shows that the scattering signature of an object can be transformed into that of another with pre-selected size and material properties. In particular, not only can the overall RCS of a coated object be either reduced or enlarged, its angular distribution can also be altered at will.

As depicted in Figure 1(c), the metasurface illusion coating design can be derived by considering a plane wave illuminating an infinitely long cylinder coated by an anisotropic metasurface incident at an arbitrary elevation angle of θ_i ($0° \le \theta_i \le 180°$). The electric field vector of the incident wave is confined to lie within the x-z plane, corresponding to a transverse magnetic (TM_z) polarization, which represents the polarization of more practical interest. The inner cylinder has a relative permittivity of ε_d and a radius of a_d, while the metasurface coating is placed at a radial distance of a_c, with its electric and magnetic surface polarizability tensors denoted as $\bar{\bar{\alpha}}_E = \left[0, \alpha_E^{\varphi}, \alpha_E^{z}\right]$ and $\bar{\bar{\alpha}}_M = \left[\alpha_M^{\rho}, 0, 0\right]$, respectively. The ρ component of $\bar{\bar{\alpha}}_E$, and the φ and z components of $\bar{\bar{\alpha}}_M$ can be well-approximated by setting them to zero considering that the metasurface has a near-zero electrical thickness and does not contain any magnetic materials. An annular spacer comprised of material with a relative permittivity of ε_s and a relative permeability of μ_s is assumed to fill the region between the inner cylinder and the metasurface. Under the assumption that the time dependence is $e^{j\omega t}$, the longitudinal field components, i.e., the z components, of the electromagnetic field in the three regions (0, I, and II) can be expressed as a superposition of cylindrical harmonics[37]

$$
\begin{aligned}
E_z^0 &= E_z^i + E_z^s = \sin\theta_i \sum_{n=-\infty}^{+\infty} \left(J_n(k_{t0}\rho) + b_n^s H_n^{(2)}(k_{t0}\rho) \right) F_n \\
E_z^I &= \sin\theta_i \sum_{n=-\infty}^{+\infty} \left(a_n J_n(k_{tI}\rho) + b_n Y_n(k_{tI}\rho) \right) F_n \\
E_z^{II} &= \sin\theta_i \sum_{n=-\infty}^{+\infty} \left(a_{nII} J_n(k_{tII}\rho) \right) F_n \\
H_z^0 &= H_z^s = (\sin\theta_i/\eta_0) \sum_{n=-\infty}^{+\infty} \left(d_n^s H_n^{(2)}(k_{t0}\rho) \right) F_n \\
H_z^I &= (\sin\theta_i/\eta_I) \sum_{n=-\infty}^{+\infty} \left(c_n J_n(k_{tI}\rho) + d_n Y_n(k_{tI}\rho) \right) F_n \\
H_z^{II} &= (\sin\theta_i/\eta_{II}) \sum_{n=-\infty}^{+\infty} \left(c_{nII} J_n(k_{tII}\rho) \right) F_n ,
\end{aligned}
\tag{1}
$$

where $F_n = j^{-n} e^{jk_z z} e^{jn\varphi}$ and $k_z = k_0 \cos\theta_i$ is the longitudinal wave number. J_n and Y_n are the n^{th} order cylindrical Bessel functions of the first and second kind, respectively, and $H_n^{(2)}$ is the n^{th} order cylindrical Hankel function of the second kind. η_m and k_{tm} (m = 0, I, II) represent the characteristic impedance of the material and the transverse wave number in Region 0,

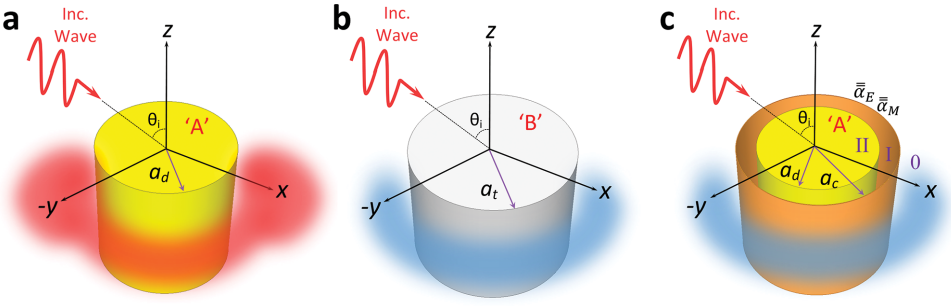

Figure 1. Schematics of the metasurface illusion. a) A cylinder comprised of material 'A' with a radius of a_d possesses a different scattering signature compared to that of b) a cylinder comprised of material 'B' with a radius of a_t. c) By coating the cylinder in (a) with a custom designed metasurface having surface polarizability tensors $\bar{\bar{\alpha}}_E$ and $\bar{\bar{\alpha}}_M$ located at a radius of a_c, the same scattering signature as that of the cylinder in (b) can be achieved.

I, and II, respectively. Based on the expressions given in (1), the ρ and φ components of the fields can be readily obtained from Maxwell's equations.[37] It should be noted that the non-vanishing z component of the magnetic field is a natural outcome of cross-polarization coupling due to the asymmetry as seen by an obliquely incident wave.[38] Considering that the surface polarizability tensors of the metasurface are anisotropic, the tangential magnetic fields on both sides of the metasurface are not continuous and thereby can be accurately described by the following second order boundary conditions:[39,40]

$$\begin{aligned}
&\hat{\rho}\times\hat{z}(H_z^0-H_z^I)\mid_{\rho=a_c}\\
&=j\omega\varepsilon_0\alpha_E^{\varphi}\left(\hat{\varphi}\frac{E_\varphi^0+E_\varphi^I}{2}\right)\Bigg|_{\rho=a_c}-\hat{\rho}\times\hat{z}\frac{\partial}{\partial z}\left(\alpha_M^{\rho}\frac{H_\rho^0+H_\rho^I}{2}\right)\Bigg|_{\rho=a_c}\\
&\hat{\rho}\times\hat{\varphi}(H_\varphi^0-H_\varphi^I)\mid_{\rho=a_c}\\
&=j\omega\varepsilon_0\alpha_E^{z}\left(\hat{z}\frac{E_z^0+E_z^I}{2}\right)\Bigg|_{\rho=a_c}-\hat{\rho}\times\hat{\varphi}\frac{1}{\rho}\frac{\partial}{\partial z}\left(\alpha_M^{\rho}\frac{H_\rho^0+H_\rho^I}{2}\right)\Bigg|_{\rho=a_c}.
\end{aligned}\tag{2}$$

By enforcing the above equations and the additional boundary conditions for continuity of the tangential electric and magnetic fields at the surface of the inner cylinder and the electric fields at the outer metasurface, the Mie scattering coefficients b_n^s and d_n^s (n = 0, 1, 2, ...) for all the scattering harmonic modes can be determined, where d_0^s is always zero. At normal incidence ($\theta_i = 90°$), d_n^s vanishes since there is no induced cross-polarization, while b_n^s reduces to

$$b_n^s=\frac{\begin{vmatrix} J_n(k_{II}a_d) & J_n(k_Ia_d) & Y_n(k_Ia_d) & 0\\ J_n'(k_{II}a_d)/\eta_{II} & J_n'(k_Ia_d)/\eta_I & Y_n'(k_Ia_d)/\eta_I & 0\\ 0 & J_n(k_Ia_c) & Y_n(k_Ia_c) & J_n(k_0a_c)\\ 0 & J_n'(k_Ia_c)/\eta_I-X_sJ_n(k_Ia_c) & Y_n'(k_Ia_c)/\eta_I-X_sY_n(k_Ia_c) & J_n'(k_0a_d)/\eta_0 \end{vmatrix}}{\begin{vmatrix} J_n(k_{II}a_d) & J_n(k_Ia_d) & Y_n(k_Ia_d) & 0\\ J_n'(k_{II}a_d)/\eta_{II} & J_n'(k_Ia_d)/\eta_I & Y_n'(k_Ia_d)/\eta_I & 0\\ 0 & J_n(k_Ia_c) & Y_n(k_Ia_c) & H_n^{(2)}(k_0a_c)\\ 0 & J_n'(k_Ia_c)/\eta_I-X_sJ_n(k_Ia_c) & Y_n'(k_Ia_c)/\eta_I-X_sY_n(k_Ia_c) & H_n^{(2)'}(k_0a_c)/\eta_0 \end{vmatrix}}\tag{3}$$

$$X_s=\omega\varepsilon_0\alpha_E^{z}+\frac{n^2\alpha_M^{\rho 2}}{2\omega a_c^2}\left(\frac{1}{\mu_0}+\frac{1}{\mu_s}\right),\tag{4}$$

where the prime notation for J_n', Y_n', and $H_n^{(2)'}$ represent derivatives with respect to the arguments. For the case where the coated cylinder is comprised of a conductor, such as copper or gold, the same equations can be employed in the asymptotic limit by allowing the value of ε_d to approach $-j\infty$. For a cylinder with a small to moderate size diameter, only the zeroth and first order Mie coefficients contribute to the scattered fields. Due to the lack of a radial magnetic field component for the zeroth order scattering mode, b_0^s is controlled solely by α_E^z of the metasurface, while the remaining coefficients d_0^s, b_1^s, and d_1^s can be affected by any of the three surface polarizability tensor parameters (α_E^z, α_E^{φ}, and α_M^{ρ}). As a result, by changing the values of a_c, ε_s, $\bar{\bar{\alpha}}_E$, and $\bar{\bar{\alpha}}_M$, both the real and imaginary parts of b_n^s and d_n^s can be tailored such that they are equated to those of another object within a certain range of the incident angle, thus achieving the desired angle-tolerant electromagnetic illusion effect. This enables an unprecedented capability for scattering manipulation using practical ultrathin metasurfaces, which is more general and versatile than cloaking where only the magnitudes of the Mie coefficients are suppressed.[19–21] It should be noted that higher order scattering modes will come into play as the diameter of the cylinder to be coated increases, resulting in an additional number of metasurface layers in order to achieve effective manipulation of all the scattering modes.

3. Angle-tolerant Metasurface Illusion for Dielectric Cylinders

3.1. Analytical and Numerical Results for Infinite Dielectric Cylinders

We first illustrate how a metasurface-coated dielectric cylinder can be designed to mimic a conducting cylinder with a larger physical size and thus a stronger RCS. The targeted conducting cylinder is comprised of copper with a diameter of $d_t = 0.317\lambda_0$ at 2.5 GHz, while the Teflon cylinder to be coated has a radius of $2a_d = 0.212\lambda_0$ and a relative permittivity of 2.1. Such a diameter value is chosen since it falls into the size range of a practical sensor or antenna. In order to mimic the scattering signature of the copper cylinder within a certain range of the incidence angle ($80° \le \theta_i \le 100°$), the simplest method is to shield the Teflon cylinder with a conducting sheet placed at the exact radius of $d_t/2$. However, this completely isolates the region inside the shielding from the outside world, making it undesired for sensing or probing applications. By using an anisotropic metasurface, however, the illusion effect can be achieved with a coating that has a lower profile than d_t, all while permitting communication between the interior of the metasurface coating and the outside world. This is significantly different from previously demonstrated TO-enabled illusion devices where the inhomogeneous and anisotropic material coating has a much larger profile than the targeted object. The values of a_c, $\bar{\bar{\alpha}}_E$, and $\bar{\bar{\alpha}}_M$ were obtained by applying a robust global optimization scheme known as the covariance matrix adaptation evolutionary strategy (CMA-ES) to minimize the mean square error fit between the resulting RCS patterns and those of the targeted copper cylinder within the $80° \le \theta_i \le 100°$ incident angle range.[41,42] The optimized parameters of the metasurface coating were found to be $a_c = 0.278\lambda_0$, $\alpha_E^z/\lambda_0 = 1.352$, and $\alpha_M^{\rho}/\lambda_0 = 0.168$. The $\lambda_0/30$ thick spacer was set to be a layer of foam with $\varepsilon_s = 1.06$, and the value of $\alpha_E^{\varphi}/\lambda_0$ can be arbitrarily chosen as long as it is smaller than 0.5 since it has a negligible effect on the scattering signature compared to the other parameters. **Figures 2**(a)–2(c) compare the electric-field distributions for the three structures under plane wave excitation at normal incidence ($\theta_i = 90°$): a bare copper cylinder, a bare Teflon cylinder, and the metasurface-coated Teflon cylinder. It can be seen that the metasurface-coated Teflon cylinder produces a field distribution almost the same as that of the copper cylinder both qualitatively and quantitatively. Physically, the surface currents induced on the metasurface are engineered to properly interfere with the fields induced inside the inner Teflon cylinder, giving rise to the altered scattered fields.[36] The far-zone bistatic RCS patterns for both normal incidence and oblique incidence

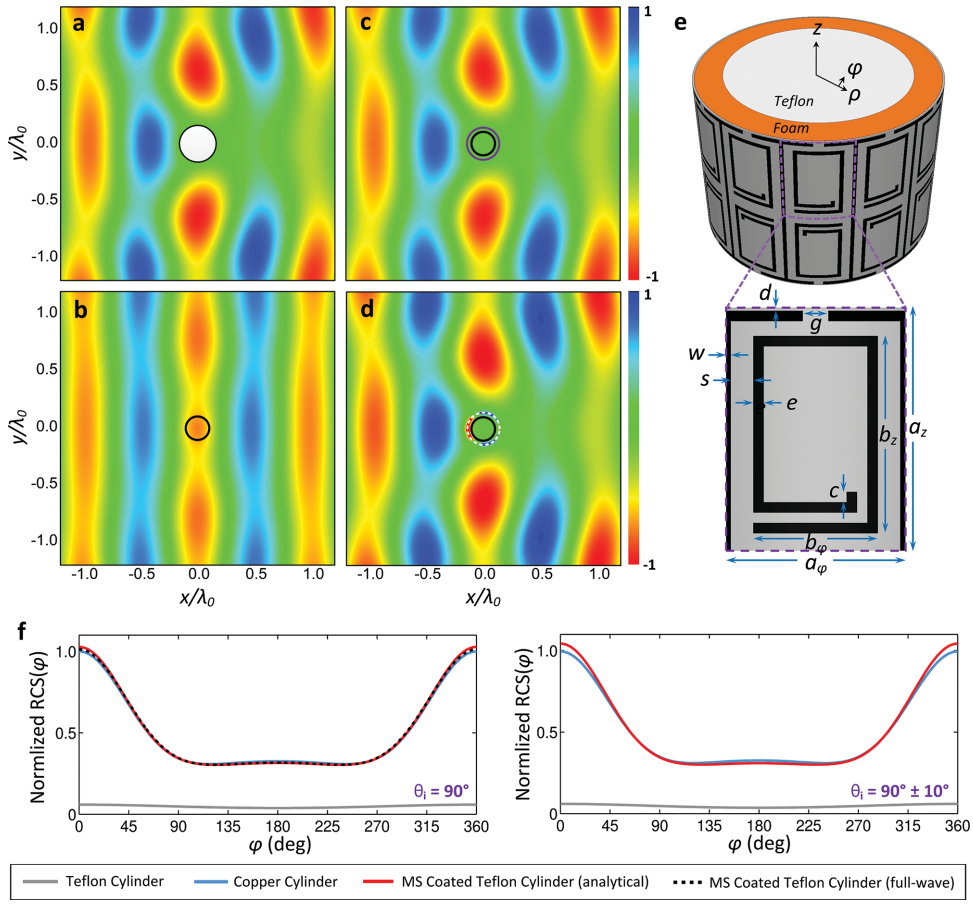

Figure 2. Transforming the scattering signature of an infinitely long dielectric cylinder into that of an infinitely long conducting cylinder. Snapshots of the analytically calculated total ***E***-field distribution for a) the targeted copper cylinder, b) the uncoated Teflon cylinder, and c) the same Teflon cylinder coated by the custom designed metasurface. d) Snapshots of the total ***E***-field distribution for the Teflon cylinder coated by the custom designed metasurface evaluated using full-wave simulations. e) Configuration of the metasurface coating and its associated unit cell. The dimensions are $a_z = 11.723$, $a_\phi = 8.744$, $b_z = 9.5$, $b_\phi = 6$, c = 0.5, $d = 0.1$, $e = 0.5$, $g = 1.24$, $s = 0.75$, and $w = 0.25$ (all in millimeters). f) The analytically calculated and full-wave simulated far-field RCS patterns of the targeted copper cylinder, the Teflon cylinder, and the Teflon cylinder coated with the homogenous and discrete metasurface for normal and ±10° oblique incidence angles.

with $\theta_i = 80°$ are displayed in Figure 2(f), which are collected at an elevation angle of $180°-\theta_i$ and normalized to the peak RCS value of the targeted copper cylinder at normal incidence. It can be seen that the RCS patterns produced by the Teflon cylinder coated with the metasurface agree well with those of the copper cylinder, with an average deviation of only 1.85% at normal incidence and 3.05% at ±10° oblique incidence angles. At larger incidence angles of ±20°, the deviation is slightly increased to 4.72%.

To realize the required electromagnetic properties of the illusion coating, an artificially engineered metasurface composed of electric and magnetic unit cells is proposed, which is a composite array of capacitively coupled short dipole and spiral resonator (CCSD-SR) elements, as illustrated in Figure 2(e). The CCSDs provide the in-plane electric response while the SRs yield the desired longitudinal magnetic properties.[43–45] The unit cell contains a pair of CCSD-SRs printed on one side of a 0.5 mm ($\sim\lambda_0/240$ at 2.5 GHz) thick low-loss printed circuit board material (Rogers RT/duroid 5880) with a relative permittivity $\varepsilon_r = 2.2 - j0.0019$. The unit cell width ($\alpha_\phi$) was set to be 8.74 mm such that twelve cells can fit around the 104.88 mm long circumference of the coating. The dimensions of the CCSD and SR were optimized to provide the desired surface electric and magnetic polarizability properties. During the unit cell design process, a high frequency structure simulator (HFSS) solver was employed to perform the full-wave scattering calculations for a plane-wave at different angles of incidence. The relevant effective surface polarizability tensor parameters (α_E^z, α_M^ρ, and α_E^φ) were then retrieved from the complex reflection and transmission coefficients (see Supporting Information). Figure 2(d) reports the electric-field distribution for the Teflon cylinder coated by the realistic metasurface under plane wave illumination at normal incidence. In the HFSS simulation domain, a metasurface-coated Teflon cylinder with a height equal to the length of one unit cell ($2a_z$) is sandwiched between a parallel plate waveguide to mimic an infinitely long structure. By comparing Figure 2(c) and 2(d), excellent agreement can be observed between the electric-field distribution obtained from the analytical expressions for the homogeneous metasurface (e.g., based on an effective medium representation) and that

calculated by the full-wave simulation of the discrete metasurface, implying that the designed CCSD-SR composite array indeed behaves as an effective homogeneous metasurface. Due to the fact that the unit cells of the metasurface operate at frequencies away from the resonance and only a monolayer is employed, the resulting illusion coating has negligible absorption loss. Furthermore, it should be noted that a finite non-zero electric field is induced inside the Teflon cylinder (although very weak), indicating that the cylinder is not isolated from the outside region. Figure 2(f) displays the bistatic RCS pattern of the discrete metasurface coated infinitely long Teflon cylinder at normal incidence, which is normalized to the maximum value of the RCS of the targeted copper cylinder at normal incidence. It can be seen that the scattering signature is greatly enhanced by the presence of the synthesized metasurface coating comprised of actual sub-wavelength patterned metallic unit cells, closely mimicking that of the targeted copper cylinder with an average deviation of only 1.52%. Further investigations of this illusion coating under a cylindrical wave excitation at different distances away from the object show that the desired illusion functionality is well maintained (see Figure S2), confirming the robustness of the metasurface to excitations with different waveforms.

3.2. Numerical and Experimental Results for Finite Dielectric Cylinder

To experimentally verify the concept and the design proposed above, a practical finite-length Teflon cylinder is employed. Here, the length of the Teflon cylinder is truncated to 28.1 cm, i.e., ~$2.34\lambda_0$ at 2.5 GHz, which is slightly offset from multiples of a half wavelength to avoid undesired resonances.[46] **Figure 3**(a) shows the configuration of the finite-length Teflon cylinder coated by the designed single layer metasurface with 12 unit cells along the direction of the cylinder axis. The cylinder is tilted with an angle θ_{tilt} from the z-axis in the x-z plane while the incident wave is propagating in the $+x$ direction (i.e., $\theta_i = 90°$) with its electric field polarized in the z direction. With the aid of the HFSS full-wave solver, the length of the spiral trace was trimmed by 3 mm to compensate for the diffraction that occurred at the top and bottom ends of the cylinder and the metasurface. Figure 3(c) and 3(d) show the simulated far-field RCS patterns in the x-y plane for the three cases – the targeted finite-length copper cylinder and the finite-length Teflon cylinder with and without the modified metasurface coating – with $\theta_{tilt} = 0°$ and 10°, respectively. Since the structures are symmetrical about the x-z plane, only the range $0° \le \phi \le 180°$ is shown. The RCS patterns are normalized to the simulated peak RCS value of the targeted finite-length copper cylinder at normal incidence, i.e., $\theta_{tilt} = 0°$. It can be seen that the metasurface coating significantly increases the scattered field intensity, resulting in RCS patterns that correspond well to those of the finite-length copper cylinder with average deviations of 2.25%

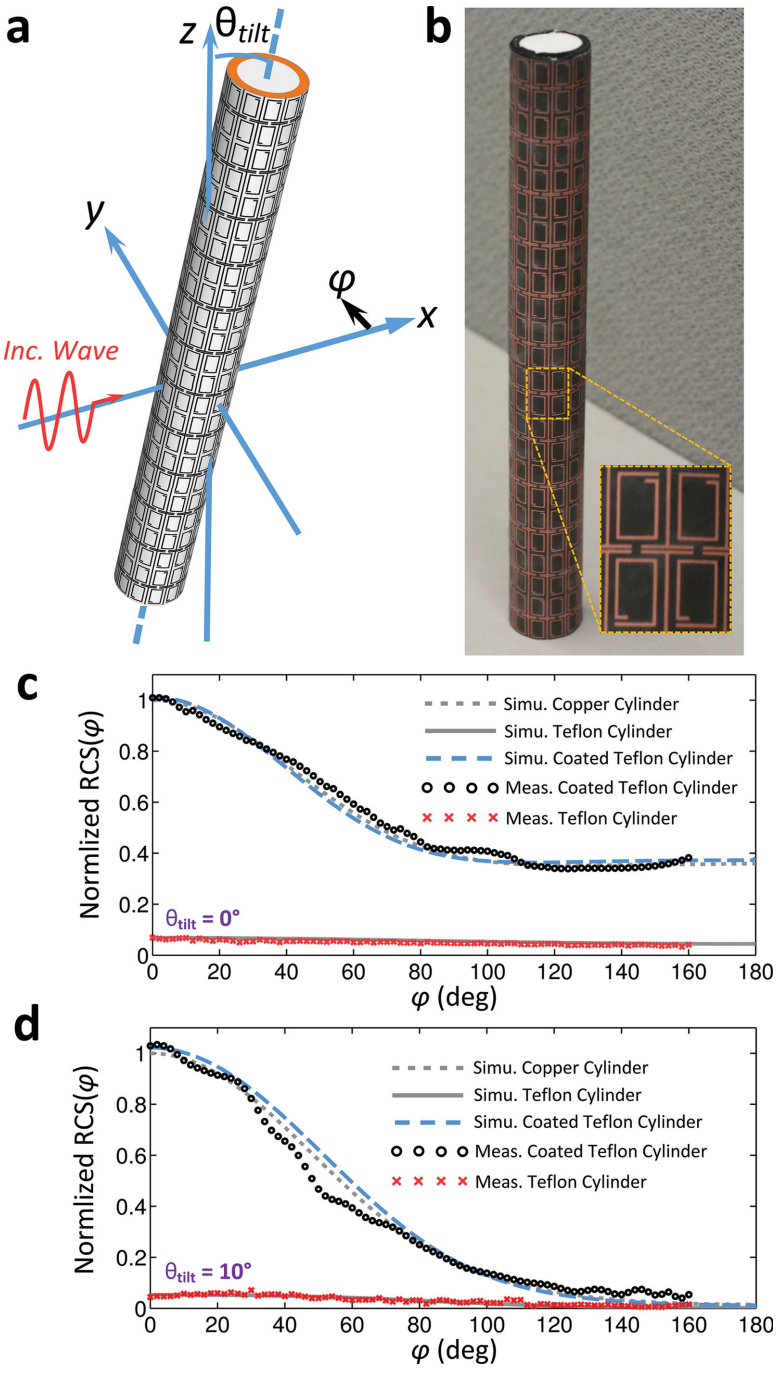

Figure 3. Simulation and experimental validation of the illusion effect for a finite-length dielectric cylinder. a) Configuration of the finite-length Teflon cylinder coated by the discrete metasurface with a tilting angle θ_{tilt} from the z-axis. The incident wave is propagating along the $+x$ direction and polarized in the z-direction. b) Photographs of the fabricated metasurface coating prototype. The inset shows enlarged unit cells of the sample. Full-wave simulated and measured far-field RCS patterns in the horizontal (x-y) plane for the Teflon cylinder with and without the metasurface coating where c) $\theta_{tilt} = 0°$ and (d) $\theta_{tilt} = 10°$.

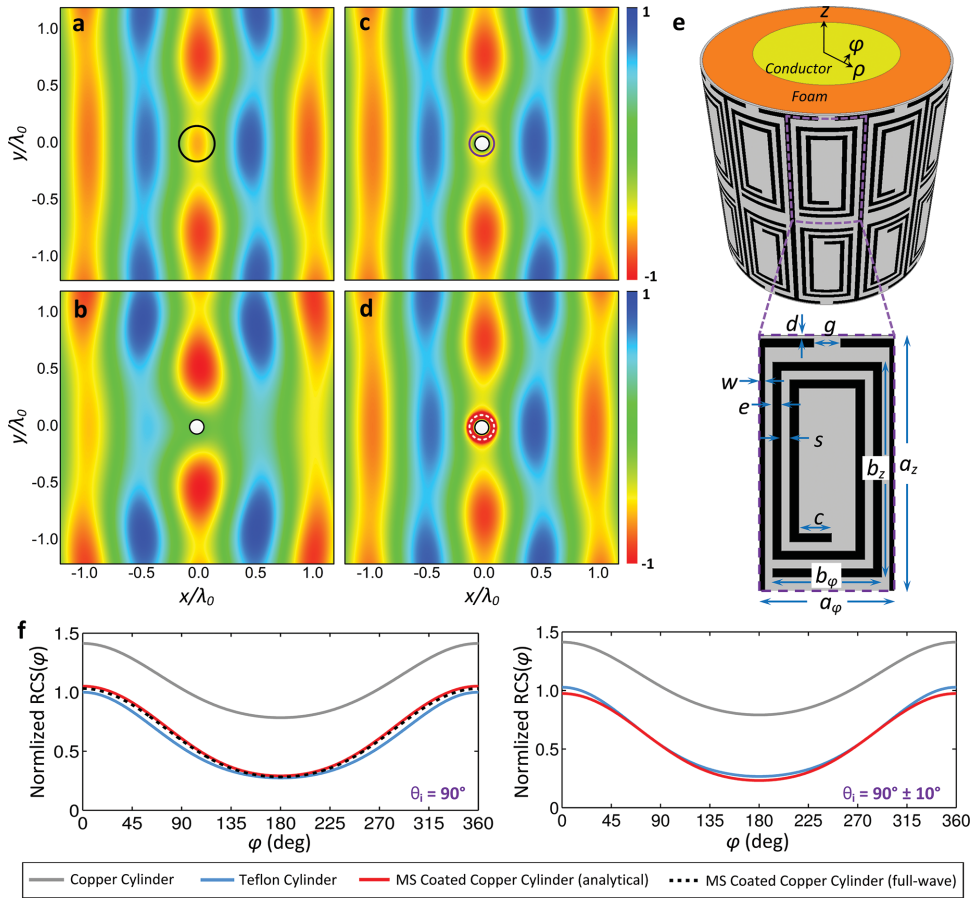

Figure 4. Transforming the scattering signature of an infinitely long conducting cylinder into that of an infinitely long dielectric cylinder. Snapshots of the analytically calculated total ***E***-field distribution for a) the targeted Teflon cylinder, b) the uncoated copper cylinder, and c) the same copper cylinder coated by the custom designed metasurface. d) Snapshots of the total ***E***-field distribution for the copper cylinder coated by the custom designed metasurface evaluated using full-wave simulations. e) Configuration of the metasurface coating and its associated unit cell. The dimensions are $a_z = 11.723$, $a_\phi = 6.39$, $b_z = 9.7$, $b_\phi = 5$, c = 0.7, $d = 0.18$, $e = 0.4$, $g = 1.59$, $s = 0.4$, and $w = 0.25$ (all in millimeters). f) The analytically calculated and full-wave simulated far-field RCS patterns of the targeted Teflon cylinder, the copper cylinder, and the copper cylinder coated with the homogenous and discrete metasurface for normal and ±10° oblique incidence angles.

and 4.17% for normal and ±10° oblique incidence angles, respectively. This illusion effect is also manifested in the three-dimensional far-field RCS patterns (see Figure S3), indicating that such metasurface illusion coatings not only work for infinite objects, which are inherently two-dimensional, but can be effectively extended to quasi-three-dimensions for the practical case of finite-length objects.[23–27] In addition, it has a certain angular tolerance such that the three-dimensional illusion effect is well maintained within a field-of-view up to ±10° off normal.

The metasurface coating was fabricated and wrapped around a 28.1 cm long Teflon cylinder, as shown in Figure 3(b). Four layers of foam, each with a thickness of 1 mm, were stacked as a spacer in between the metasurface and the Teflon cylinder. The bistatic RCS patterns of the Teflon cylinder with and without the metasurface coating in the horizontal (x-y) plane were measured in an anechoic chamber using two horn antennas. They were normalized to the simulated peak RCS value of the targeted copper cylinder at normal incidence. Due to the finite size of the horn antennas, the scattering information within the 160° ≤φ ≤ 200° angular range could not be obtained. As presented in Figure 3(c) and 3(d), very good agreement between simulations and measurements is observed, showing greatly enhanced scattering due to the metasurface coating. The resulting angular distributions of the RCS closely mimic those of the targeted copper cylinder. With the metasurface coating, the measured RCS patterns exhibit average deviations of 3.58% and 6.97% from the simulated results of the targeted copper cylinder at normal and ±10° oblique incidence angles, respectively. The small discrepancies between simulation and measurement are attributed to fabrication inaccuracies and measurement noise. In all, the experiments validate that the anisotropic metasurface indeed manipulates the scattering perception of a finite-length dielectric object and electromagnetically transforms it into that of a conducting cylinder.

4. Angle-tolerant Metasurface Illusion for Conducting Cylinders

The example presented above demonstrates that a metasurface can transform the scattering signature of an object into that of

another stronger scatterer. To further demonstrate the versatility of the general approach, we next show that a metasurface coating can also be designed to change the scattering response of an object to mimic that of another with a weaker signature. Here, the targeted cylinder is comprised of Teflon with a diameter of $d_t = 0.317\lambda_0$ at 2.5 GHz and a relative permittivity of 2.1, while the cylinder to be coated is made of copper with a radius of $2a_d = 0.12\lambda_0$. The optimized geometrical and material parameters of the metasurface coating for achieving the illusion effect (i.e., making the copper cylinder look like a Teflon cylinder) are $a_c = 0.1\lambda_0$, $\alpha_E^z/\lambda_0 = 0.643$, and $\alpha_M^\rho/\lambda_0 = -0.09$. A CCSD-SR composite array with 12 elements in the ϕ direction was designed to realize the desired superficial electromagnetic properties, as shown in **Figure 4**(e). Figure 4(a)-(d) compare the electric-field distributions for the four structures under plane wave excitation at normal incidence ($\theta_i = 90°$): a bare Teflon cylinder, a bare copper cylinder, the copper cylinder coated with the homogeneous metasurface and the discrete metasurface. It can be seen that the metasurface-coated copper cylinder produces weaker scattered fields than in the case without the coating, resulting in a field distribution almost the same as that of the targeted Teflon cylinder. The far-zone bistatic RCS patterns for both normal and ±10° oblique incidence angles are displayed in Figure 4(f), which are normalized to the simulated peak RCS value of the targeted Teflon cylinder at normal incidence. It is found that the RCS patterns of the infinitely long copper cylinder coated with the metasurface correspond well to those of the Teflon cylinder, with average deviations of only 4.81% and 4.26% at normal incidence for the homogenous and discrete metasurfaces, respectively, and 3.93% at ±10° oblique incidence angles for the homogenous metasurface. Importantly, non-vanishing surface currents are induced on the inner copper cylinder, indicating that the electromagnetic wave from the outside world is not shielded from the object on the interior. Moreover, the metasurface retains its ability to perform the illusion effect for the conducting cylinder under a cylindrical wave excitation at various distances away from the object (see Figure S4).

To experimentally verify this design, a finite 28.1 cm long copper cylinder was used. As shown in **Figure 5**(a), the length of the spiral trace was increased by 2.5 mm to compensate for the edge diffraction that occurred at the top and bottom of the structure. The simulated RCS patterns, normalized to the maximum value of the RCS of the targeted Teflon cylinder at normal incidence, are displayed in Figure 5(c) and 5(d). It can be seen that even for such a highly truncated copper cylinder, the metasurface was able to reduce the strength of its scattered field in the horizontal plane to mimic

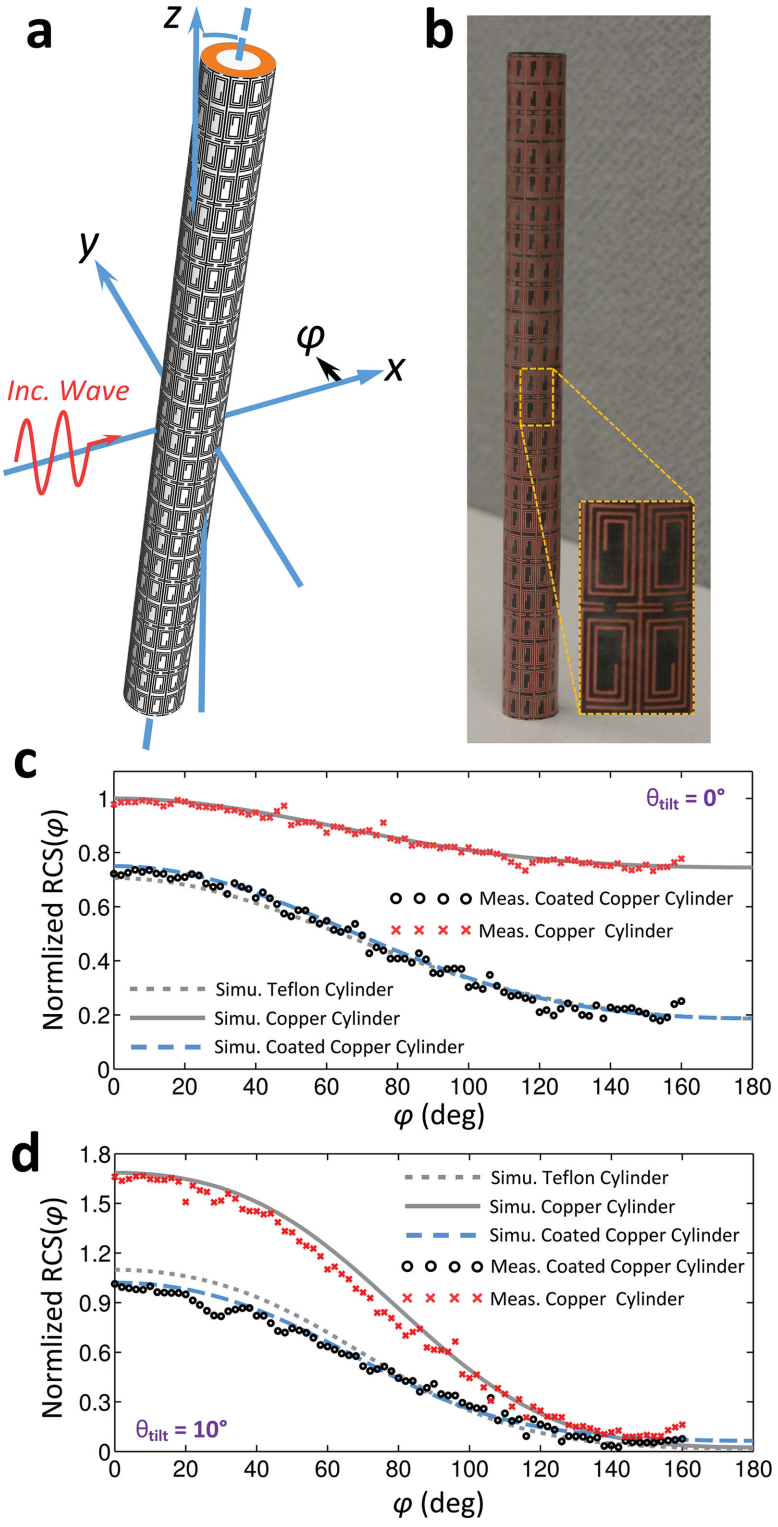

Figure 5. Simulation and experimental validation of the illusion effect for a finite-length conducting cylinder**.** a) Configuration of the finite-length copper cylinder coated by the discrete metasurface with a tilting angle θ_{tilt} from the *z*-axis. The incident wave is propagating along the +*x* direction and polarized in the *z*-direction. b) Photographs of the fabricated metasurface coating prototype. The inset shows enlarged unit cells of the sample. Full-wave simulated and measured far-field RCS patterns in the horizontal (*x*-*y*) plane for the copper cylinder with and without the metasurface coating where c) θ_{tilt} = 0° and (d) θ_{tilt} = 10°.

the RCS patterns of the targeted Teflon cylinder with the same length. The average deviations are 4.35% and 7.68% for 0° and 10° tilting angles, respectively. Similar to the first example, the full illusion effect is well manifested in the three-dimensional RCS patterns (see Figure S5). The metasurface was fabricated (see Figure 5(b)) and its RCS patterns in the horizontal plane were measured for both tilting angles. As displayed in Figure 5(c) and 5(d), the simulated and measured RCS patterns exhibit good agreement. Quantitatively, with the metasurface coating, the measured scattering patterns show a 5.19% and 11.79% deviation from the simulated results of the targeted Teflon cylinder at normal and ±10° oblique incidence angles, respectively. This demonstrates that, in addition to enhancing the scattered field, the single layer metasurface illusion coating can also be designed to effectively transform the perceived scattering signature of an object into another that is weaker, thereby confirming the versatility of the general theory and design approach.

5. Conclusions

In summary, we have presented the theory, practical design, and experimental verification of quasi-three-dimensional angle-tolerant electromagnetic illusion effects enabled by ultrathin metasurface coatings. The demonstrated approach provides a methodology for transforming the scattering signature of an object into that of another which has been pre-selected by the designer. Importantly, the desired illusion effects are realized by an ultrathin single-layer anisotropic metasurface coating, thereby enabling light-weight and low-profile devices, all while allowing for communications between the coated object and the outside world. The functional metasurfaces with non-vanishing radial electromagnetic response were realized by a CCSD-SR composite array. Two examples have been demonstrated at microwave frequencies, creating quasi-three-dimensional illusions for both finite-length dielectric and copper cylinders with small deivations within a ±10° field-of-view. The concept and the general design approach presented here can be readily extended to metasurface illusion coatings operating in the terahertz range[20] and even possibly at optical wavelengths.[47]

6. Experimental Section

RCS Pattern Measurement: The RCS patterns of the finite-length Teflon/copper cylinders with and without the metasurface coating in the horizontal (*x*-*y*) plane were characterized in an anechoic chamber. Two double-ridged S-band horn antennas connected by a vector network analyzer were employed – one with a fixed position as the transmitter and the other moving around the cylinder in the horizontal plane as the receiver. Both horn antennas were 1.2 m, ~ 10 λ_0, away from the cylinder with their transmitted/received electric field polarized in the *z*-direction. Due to the finite size of the horn antennas, RCS information within the angular range of $160° \le \phi \le 200°$ was not available. The complex transmission coeffcient, $S_{21b}(f,\phi)$, between the two horn antennas without the presence of any object was recorded as the background signal. The scattering signal of the object, $S_{21s}(f,\phi)$, was obtained by removing $S_{21b}(f,\phi)$ from the complex transmission coefficient ($S_{21}(f, \phi)$) measured with the presence of the object as $S_{21s}(f,\phi) = S_{21}(f,\phi) - S_{21b}(f,\phi)$. The RCS was then calculated by $RCS(f,\phi) = (4\pi)^3 R^4 |S_{21s}(f,\phi)|^2 / (G_t G_r (\lambda_0)^2)$ where R is the distance between the target and the receiving/transmitting anatenna, while G_t and G_r are the absolute gains of the tranmitting and receiving antennas, respectively.[37]

Supporting Information

Supporting Information is available from the Wiley Online Library or from the author.

Acknowledgements

This work was supported by a NSF MRSEC under Grant DMR-0820404. The authors would like to thank Clinton P. Scarborough for his help in the experimental setup.

Received: May 14, 2014
Revised: August 6, 2014
Published online: October 9, 2014

[1] N. Engheta, R. Ziolkowski, *Metamaterials: Physics and Engineering Explorations*, Wiley-IEEE Press, Hoboken, NJ, USA **2006**.
[2] T. J. Cui, D. R. Smith, R. Liu, *Metamaterials–Theory, Design, and Applications*, Springer, London, UK **2009**.
[3] D. H. Werner, D.-H. Kwon, *Transformation Electromagnetics and Metamaterials: Fundamental Principles and Applications*, Springer, London, UK **2014**.
[4] J. B. Pendry, D. Schurig, D. R. Smith, *Science* **2006**, *312*, 1780.
[5] D. Schurig, J. J. Mock, B. J. Justice, S. A. Cummer, J. B. Pendry, A. F. Starr, D. R. Smith, *Science* **2006**, *314*, 977.
[6] R. Liu, C. Ji, J. J. Mock, J. Y. Chin, T. J. Cui, D. R. Smith, *Science* **2009**, *323*, 366.
[7] J. Valentine, J. Li, T. Zentgraf, G. Bartal, X. Zhang, *Nat. Mater.* **2009**, *8*, 568.
[8] L. H. Gabrielli, J. Cardenas, C. B. Poitras, M. Lipson, *Nat. Photonics* **2009**, *3*, 461.
[9] H. F. Ma, T. J. Cui, *Nat. Commun.* **2010**, *1*, 21.
[10] D.-H. Kwon, D. H. Werner, *Appl. Phys. Lett.* **2008**, *92*, 013505.
[11] A. Greenleaf, Y. Kurylev, M. Lassas, G. Uhlmann, *Phys. Rev. E* **2011**, *83*, 016603.
[12] A. Alù, N. Engheta, *Phys. Rev. Lett.* **2009**, *102*, 233901.
[13] A. Alù, N. Engheta, *Phys. Rev. E* **2005**, *72*, 016623.
[14] M. G. Silveirinha, A. Alù, N. Engheta, *Phys. Rev. E* **2007**, *75*, 036603.
[15] C.-W. Qiu, L. Hu, X. Xu, Y. Feng, *Phys. Rev. E* **2009**, *79*, 047602.
[16] D. Rainwater, A. Kerkhoff, K. Melin, J. C. Soric, G. Moreno, A. Alù, *N. J. Phys.* **2012**, *14*, 013054.
[17] S. Tretyakov, P. Alitalo, O. Luukkonen, C. Simovski, *Phys. Rev. Lett.* **2009**, *103*, 103905.
[18] A. Alù, *Phys. Rev. B* **2009**, *80*, 245115.
[19] P. Y. Chen, A. Alù, *Phys. Rev. B* **2011**, *84*, 205110.
[20] P. Y. Chen, A. Alù, *ACS Nano* **2011**, *5*, 5855.
[21] J. C. Soric, P. Y. Chen, A. Kerkhoff, D. Rainwater, K. Melin, A. Alù, *N. J. Phys.* **2013**, *15*, 033037.
[22] Y. Lai, H. Y. Chen, D. Z. Han, J. J. Xiao, Z.-Q. Zhang, C. T. Chan, *Phys. Rev. Lett.* **2009**, *102*, 253902.
[23] W. X. Jiang, H. F. Ma, Q. Cheng, T. J. Cui, *Appl. Phys. Lett.* **2010**, *96*, 121910.
[24] C. Li, X. K. Meng, X. Liu, F. Li, G. Y. Fang, H. Y. Chen, C. T. Chan, *Phys. Rev. Lett.* **2010**, *105*, 233906.
[25] W. X. Jiang, T. J. Cui, *Phys. Rev. E* **2011**, *83*, 026601.
[26] W. X. Jiang, C.-W. Qiu, T. Han, S. Zhang, T. J. Cui, *Adv. Funct. Mater.* **2013**, *23*, 4028.

[27] H.-X. Xu, G.-M. Wang, K. Ma, T. J. Cui, *Adv. Opt. Mater.* **2014**, *2*, 572.
[28] P. Y. Chen, J. Soric, A. Alù, *Adv. Mater.* **2012**, *24*, 281.
[29] H. Chen, C. T. Chan, P. Sheng, *Nat. Mater.* **2010**, *9*, 387.
[30] Q. Wu, Z. H. Jiang, O. Quevedo-Teruel, J. P. Turpin, W. Tang, Y. Hao, D. H. Werner, *IEEE Trans. Antennas Propagat.* **2013**, *61*, 5910.
[31] D. Bojanjac, Z. Sipus, *IEEE Trans. Antennas Propagat.* **2012**, *60*, 4814.
[32] B. Zhang, H. Chen, B.-I. Wu, Y. Luo, L. Ran, J. A. Kong, *Phys. Rev. B* **2007**, *76*, 121101.
[33] M. Kerker, *J. Opt. Soc. Am.* **1975**, *65*, 376.
[34] A. V. Kildishev, A. Boltasseva, V. M. Shalaev, *Science* **2013**, *339*, 1232009.
[35] C. L. Holloway, E. F. Kuester, J. A. Gordon, J. O'Hara, J. Booth, D. R. Smith, *IEEE Antennas Propagat. Magazine* **2012**, *54*, 10.
[36] Z. H. Jiang, D. H. Werner, *J. Phys. D Appl. Phys.* **2013**, *46*, 505306.
[37] C. A. Balanis, *Advanced Engineering Electromagnetics*, Wiley, New York, NY, USA **1989**.
[38] J. R. Wait, *Can. J. Phys.* **1955**, *33*, 189.
[39] T. B. A. Senior, *Appl. Sci. Res. B* **1960**, *8*, 418.
[40] E. F. Kuester, M. A. Mohamed, C. L. Holloway, *IEEE Trans. Antennas Propag.* **2003**, *51*, 2641.
[41] N. Hansen, A. Ostermeier, *Evol. Comput.* **2001**, *9*, 159.
[42] M. D. Gregory, Z. Bayraktar, D. H. Werner, *IEEE Trans. Antennas Propagat.* **2011**, *59*, 1275.
[43] Z. H. Jiang, M. D. Gregory, D. H. Werner, *Phys. Rev. B* **2011**, *84*, 165111.
[44] Z. H. Jiang, M. D. Gregory, D. H. Werner, *IEEE Antennas Wireless Propagat. Lett.* **2011**, *10*, 1543.
[45] Z. H. Jiang, Q. Wu, D. E. Brocker, P. E. Sieber, D. H. Werner, *IEEE Trans. Antennas Propagat.* **2014**, *62*, 1173.
[46] G. T. Ruck, D. E. Barrick, W. D. Stuart, C. K. Krichbaum, *Radar Cross Section Handbook*, Plenum, New York, NY, USA, **1970**.
[47] P. Fan, U. K. Chettiar, L. Cao, F. Afshinmanesh, N. Engheta, M. L. Brongersma, *Nat. Photon.* **2012**, *6*, 380.